

Effect of Sintering Temperature on the Structural, Magnetic and Impedance Spectroscopy of CoCuZn Ferrites Synthesized From Nanocrystalline Powder

A. Bagum, M. B. Hossen* and F.-U.-Z. Chowdhury

Department of Physics, Chittagong University of Engineering and Technology (CUET), Chittagong - 4349

ABSTRACT

The effect of sintering temperature on the structural and electromagnetic properties of $\text{Co}_{0.4}\text{Cu}_{0.2}\text{Zn}_{0.4}\text{Fe}_2\text{O}_4$ prepared by auto combustion technique has been studied. The samples are sintered at various sintering temperatures (1150, 1200 and 1250 °C). X-ray diffraction studies reveal the formation of single phase spinel type cubic structure. From the XRD studies of calcined powders, nanocrystalline phase is confirmed with crystallite size of 41 nm. The surface morphology of the samples studied by the field emission scanning electron microscopy shows that the average grain size increases with sintering temperature. The complex initial permeability spectra and relative quality factor are measured at room temperature show significant variation with the sintering temperature. The increase in permeability is observed due to increase in grain size and better densification. The complex impedance spectra have been analysed and explained using the Cole-Cole expression. The impedance analysis shows that the value of grain and grain boundary impedance decreases significantly with sintering temperature.

Keywords: CoCuZn ferrite; sintering temperature; initial permeability; impedance spectra.

1. Introduction

The synthesis of nanocrystalline ferrites has been intensively studied in recent years due to their potential applications in the high-density magnetic recording, microwave devices, magnetic fluids, magnetic drug delivery, hyperthermia for cancer treatment, etc. [1,2]. The high frequency electromagnetic devices like microwave absorbers, converters and inductors require high initial permeability at radio frequency range [3]. Ferrites are considered superior to other magnetic materials because of low eddy current losses due to high electrical resistivity, high permeability in the radio-frequency region, mechanical hardness and chemical stability [4]. Recently there is a growing interest on Co-ferrite which has peculiar properties like high saturation magnetization, high coercivity, large remanence, high chemical stability and large anisotropy [5,6]. Owing to this, it acts as a promising material in the high density magnetic recording media [7]. Cobalt ferrites have an inverse spinel structure with Co^{2+} ions in the octahedral (B) sites and Fe^{3+} ions equally distributed between

tetrahedral (A) and octahedral (B) sites. Therefore, substitution of Co^{2+} in this ferrite with various metal cations like Zn^{2+} , Ni^{2+} , Cu^{2+} etc. allows some tuneable changes in the properties [6,8-13]. The structural and magnetic properties of nano-size $\text{Cu}_{0.61-x}\text{Co}_x\text{Zn}_{0.39}\text{Fe}_2\text{O}_4$ prepared by sol-gel method was studied by Sindhu et al. [14] and found that CoCuZn ferrites have significance in magnetic recording medium since they have a high saturation magnetization and a moderately high coercivity. Several experiments suggested that the sintering temperature has a great influence on the structural and magnetic properties of ferrites [1,15-17]. In our study, we focus on the synthesis of nanocrystalline $\text{Co}_{0.4}\text{Cu}_{0.2}\text{Zn}_{0.4}\text{Fe}_2\text{O}_4$ by auto combustion method and investigate the effect of sintering temperature on the structural, magnetic and electrical properties of this ferrite as a function of frequency and impedance spectroscopy technique. Particularly noteworthy that, this will furnish magnitude of permeability and zone of utility of the material.

2. Materials and Method

The $\text{Co}_{0.4}\text{Cu}_{0.2}\text{Zn}_{0.4}\text{Fe}_2\text{O}_4$ samples were prepared by using the auto combustion method at the

* Corresponding author.

E-mail: belalcuet@gmail.com

For color version visit: <http://www.cuet.ac.bd/IJIST/index.html>

Postgraduate Lab, Department of Physics, Chittagong University of Engineering and Technology (CUET), Chittagong, Bangladesh. A.R. grade with high purity ethanol (C_2H_5OH), cobalt nitrate ($Co(NO_3)_2 \cdot 6H_2O$), zinc nitrate ($Zn(NO_3)_2 \cdot 6H_2O$), copper nitrate ($Cu(NO_3)_2 \cdot 3H_2O$) and ferric nitrate ($Fe(NO_3)_3 \cdot 9H_2O$) of E. Merck, Germany were used as starting materials. The metal nitrates were accurately weighed in stoichiometric proportion and dissolved in a minimum amount of ethanol to get a clear solution. This initial solutions were acidic and having $pH < 1$. Ammonia solution was slowly added to adjust the pH value 7 of the initial solutions. These mixed solutions were kept on a hot plate at $70^\circ C$ with continuous stirring. The solution became viscous and finally formed a very viscous brown gel. When finally all water molecules were removed from the mixture, the viscous gel began cracking. Upon further heating at temperature around $200^\circ C$ for 5 hours self-propagating combustion/ignition reaction was started within the gel and the whole gel was converted into brown-coloured burnt powder termed as a precursor in each case. The powder thus prepared were then calcined at $800^\circ C$ for 5 hours to get ferrite powder. These powders were granulated using 4 wt% PVA as a binder and uniaxially pressed at a pressure 15 kN/m^2 to form toroid (14 and 7 mm outer and inner diameter respectively) and disc. Finally the pressed samples were sintered at 1150 , 1200 and $1250^\circ C$ for 5h with heating rate $10^\circ C/\text{min}$ and cooling rate $5^\circ C/\text{min}$. The phase formation of calcined and sintered powders was identified using X-ray diffractometer (Philips X'Pert PRO XRD PW 3040) with $Cu-K\alpha$ radiation of wavelength, $\lambda = 1.54060 \text{ \AA}$ at Atomic Energy Centre, Dhaka, Bangladesh. The X-ray density was calculated according to the formula

$$\rho_x = \frac{8M}{N_A a^3} \quad (1)$$

where M is the molecular weight of composition, N_A is the Avogadro's number and a is the lattice constant. The bulk density of sintered samples was determined by

$$\rho_b = \frac{m}{V} \quad (2)$$

where m is the mass and V is the volume of the sample. The mean crystallite sizes were calculated from X-ray line broadening of the (3 1 1) diffraction peak using Scherrer's equation by taking in to

account the instrumental line broadening factor [18],

$$D_{xrd} = \frac{0.9\lambda}{\beta \cos \theta} \quad (3)$$

where λ is the wavelength of the X-rays, $\beta = \sqrt{\beta_{meas}^2 - \beta_o^2}$ is the full width at half maximum (in radians) after correcting the instrumental broadening factor, β_o , β_{meas} is the observed full width at half maximum and θ is the Bragg's angle. The porosity, P , was calculated using the formula:

$$P(\%) = ((\rho_x - \rho_b) / \rho_x) \times 100 \quad (4)$$

where ρ_b is the bulk density. The surface morphology and microstructure was investigated by using a Field Emission Scanning Electron Microscope (FESEM) (JEOL, JSM-7600F) at the Department of Glass and Ceramic Engineering, Bangladesh University of Engineering and Technology (BUET), Dhaka, Bangladesh. The average grain sizes (grain diameter) of the samples were determined from FESEM micrographs by linear intercept technique. The complex initial permeability and relative quality factor, Q , of toroid shaped samples were carried out at room temperature by a Wayne Kerr Precision Impedance Analyzer (model no. 6500B) in the frequency range of 10 kHz to 120 MHz at the Department of Physics, Bangladesh University of Engineering and Technology (BUET), Dhaka, Bangladesh. The real part of the complex initial permeability have been calculated using the following relations:

$$\mu'_i = L_s / L_o \quad (5)$$

where L_s is the self-inductance of the sample core and

$$L_o = \mu_o N^2 S / \pi \bar{d} \quad (6)$$

is derived geometrically, where L_o is the inductance of the winding coil without the sample core, N is the number of turns of the coil ($N = 4$), $S = (d \times h)$ is the area of cross section of the toroidal sample, h is the thickness, $d = (d_2 - d_1)/2$, d_1 is the inner diameter, d_2 is the outer diameter of the toroid sample and $\bar{d} = (d_1 + d_2)/2$ is the mean diameter of the toroid sample. The imaginary part of complex initial permeability is given by

$$\mu''_i = \mu'_i \times \tan \delta \quad (7)$$

The Q -factor was calculated using the relation:

$$Q = \mu'_i / \tan \delta \quad (8)$$

where $\tan \delta$ is the loss factor. The surfaces of the disc samples were made parallel during polishing. After polishing the samples were coated with silver pest as a contact material for the frequency

dependent transport property measurements using the impedance analyzer. The drive voltage of the impedance analyzer used in the present work is 0.5 V.

3. Results and Discussion

3.1 Structural characterization, density, porosity and microstructure

The XRD pattern of $\text{Co}_{0.4}\text{Cu}_{0.2}\text{Zn}_{0.4}\text{Fe}_2\text{O}_4$ is shown in Fig. 1. The peaks can be indexed to (1 1 1), (2 2 0), (3 1 1), (2 2 2), (4 0 0), (4 2 2), (5 1 1) and (4 4 0) planes of the cubic unit cell, which corresponds to the single phase spinel type cubic structure having space group Fd-3m. The lattice constant, a , of the samples sintered at 1200 °C is determined using Nelson–Riley (NR) extrapolation method by minimizing both the systematic and random error. The values of the lattice parameter obtained from each reflected plane were plotted against the Nelson–Riley function, $F(\theta)$. The extrapolation of the straight line to $F(\theta) = 0$ or $\theta = 90^\circ$ gives the accurate lattice constant as shown in Table 1. From the XRD studies of calcined powders, nanocrystalline phase is confirmed with crystallite size of 41 nm. It is observed from the Fig. 2 that there is a decrease in broadening of the (3 1 1) diffraction peak of sintered powder at higher temperature than that of calcined powder indicating the increase of grain size of sintered sample.

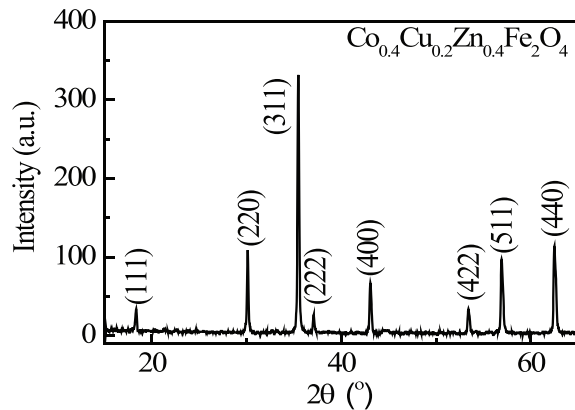


Fig. 1. X-ray diffraction pattern of $\text{Co}_{0.4}\text{Cu}_{0.2}\text{Zn}_{0.4}\text{Fe}_2\text{O}_4$ at room temperature sintered at 1200°C.

The value of X-ray density, ρ_x , of the sample is 5.31 gm/cm³. The bulk density, ρ_b , and porosity, P , of the $\text{Co}_{0.4}\text{Cu}_{0.2}\text{Zn}_{0.4}\text{Fe}_2\text{O}_4$ sample sintered at various temperature are shown in Fig. 3 and Table 1. It is seen that ρ_b increases as sintering temperature (T_s) increases and attains maximum value at 1200 °C. On the other hand, porosity of the sample shows the opposite trend of bulk density. The increase in ρ_b with

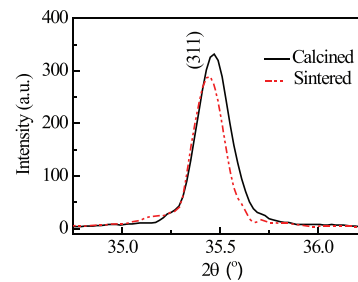


Fig. 2. Comparison of (311) peak of X-ray diffraction pattern of calcined and sintered powders of $\text{Co}_{0.4}\text{Cu}_{0.2}\text{Zn}_{0.4}\text{Fe}_2\text{O}_4$.

T_s is expected because during the sintering process, the thermal energy generates a force that drive the grain boundaries to grow over pores, thereby decreasing the pore volume and make the sample denser. A further increase of T_s at 1250 °C, the ρ_b decreases because the intragranular porosity increases resulting from the increase of thickness of grain boundary where pores or vacant sites are trapped.

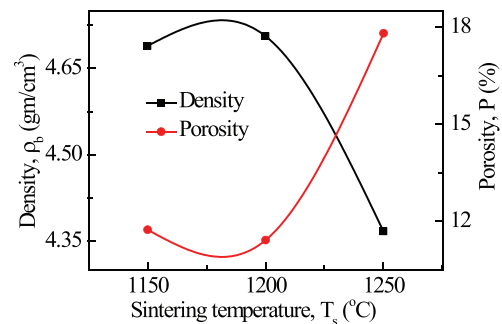


Fig. 3. The variation of ρ_b and P with various sintering temperature for $\text{Co}_{0.4}\text{Cu}_{0.2}\text{Zn}_{0.4}\text{Fe}_2\text{O}_4$.

The FESEM micrograph of $\text{Co}_{0.4}\text{Cu}_{0.2}\text{Zn}_{0.4}\text{Fe}_2\text{O}_4$ sintered at various temperatures are shown in Fig. 4. The average grain diameter, D , increases from 18.91 to 23.5 μm with increasing T_s . The uniformity in grain size can control material properties such as the magnetic permeability.

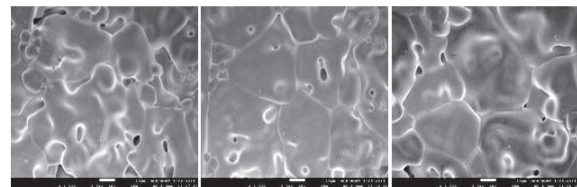


Fig. 4. The FESEM micrograph of $\text{Co}_{0.4}\text{Cu}_{0.2}\text{Zn}_{0.4}\text{Fe}_2\text{O}_4$ sintered at temperature (a) 1150 °C, (b) 1200 °C and (c) 1250 °C.

Table 1. The value of a , ρ_x , ρ_b , P and D of $\text{Co}_{0.4}\text{Cu}_{0.2}\text{Zn}_{0.4}\text{Fe}_2\text{O}_4$ sample sintered at 1150, 1200 and 1250 °C.

Sintering Temperature, T_s (°C)	Lattice constnt, a (Å)	X-ray density, ρ_x (gm/cm ³)	Bulk density, ρ_b (gm/cm ³)	Porosity, P (%)	Average grain size, D (µm)
1150	8.414	5.31	4.689	11.741	18.91
1200			4.706	11.721	22.2
1250			4.367	17.810	23.5

3.2 Complex Initial Permeability

The complex permeability spectra of $\text{Co}_{0.4}\text{Cu}_{0.2}\text{Zn}_{0.4}\text{Fe}_2\text{O}_4$ sintered at temperatures 1150, 1200 and 1250°C as a function of frequency is shown in Fig. 5. The complex permeability is given by

$$\mu_i^* = \mu_i' - i\mu_i'' \quad (9)$$

where μ_i' and μ_i'' are the real and imaginary parts of initial permeability respectively. The real permeability μ_i' describes the stored energy expressing the component of magnetic induction, B , in phase with the alternating magnetic field, H . The imaginary permeability μ_i'' describes the dissipation of energy expressing the component of B which is 90° out of phase with the alternating magnetic field.

It is observed from Fig. 5(a) that μ_i' increases with increasing T_s upto 1200°C and above $T_s = 1200^\circ\text{C}$, μ_i' decreases. The initial permeability of ferrite material depends on many factors like reversible domain wall displacement, domain wall bulging as well as microstructural features viz., average grain size, intra-granular porosity etc. [19]. In a demagnetized magnetic material there are a number of Weiss domains with Bloch walls separating two domains. These walls are bound to the equilibrium positions. The observed variations of initial permeability can be explained in terms of Globus model [20]. According to this model, the initial permeability is dependent on the grain size, saturation magnetization and magneto crystalline anisotropy as

$$\mu_i' \propto \frac{M_s^2 D}{\sqrt{K_1}} \quad (10)$$

where M_s , K_1 and D are saturation magnetization, the magnetocrystalline anisotropy constant and the average grain size respectively. According to Globus [20], the domain walls normally remain pinned to the grain boundary and bulge when subjected to a small

magnetic field. The initial permeability is mainly due to reversible motion of the domain walls. Globus assumed that the permeability due to the wall motion is likely to be linearly dependent on the grain size, while the permeability contribution due to spin rotation was assumed to be independent of grain size.

This increase of μ_i' with increasing T_s is attributed to the increase in grain size, which increases with T_s as shown in Table 1. Hence the domain wall motion becomes more significant as the sintered density and grain size of the ferrite increases. This is because bigger grains contain more domain walls and initial permeability being a result of the easy reversal of domain wall displacement in the direction of the applied magnetic field. The greater the number of domain walls, the higher is the initial permeability. At higher sintering temperature μ_i' decreases due to increase of pores in the sample as shown in Fig. 4. The pores act as pinning sites for the domain wall movement. Consequently, domain wall motion is restricted resulting in decrease of μ_i' . Furthermore, the initial permeability shows flat profile within the measured frequency range, indicating good high frequency stability. It is also observed from Fig. 5(a) that, the peak of initial permeability as well as the resonance frequency of sintered

CoCuZn ferrites are not observed in the permeability spectrum up to $f = 120$ MHz, which is the limitation of the equipment.

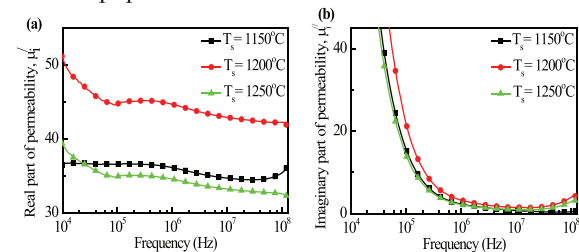


Fig. 5. (a) The real part of complex initial permeability spectra, μ_i' and (b) the imaginary part of complex initial permeability spectra, μ_i'' for $\text{Co}_{0.4}\text{Cu}_{0.2}\text{Zn}_{0.4}\text{Fe}_2\text{O}_4$ samples sintered at 1150, 1200 and 1250°C.

Fig. 5(b) shows μ_i'' as a function of frequency and it is observed that μ_i'' increases with increasing T_s up to 1200°C and after then μ_i'' decreases. At lower frequencies, the lag of domain wall motion with respect to the applied magnetic field is responsible for magnetic loss and at higher frequencies, a rapid decrease in loss factor is observed. A resonance loss peak is absent in whole measured frequency range.

Fig. 6 shows variation of relative quality factor, Q , for $\text{Co}_{0.4}\text{Cu}_{0.2}\text{Zn}_{0.4}\text{Fe}_2\text{O}_4$ sintered at temperatures 1150, 1200 and 1250 °C as a function of frequency. It is found from Fig. 6 that the Q -factor of all samples increases initially, reaching to a maximum value and then decreases rapidly with frequency. The rapid decrease shows the tendency for a resonance phenomena connected with decrease of μ_i' and subsequent increase of μ_i'' , the imaginary loss component of complex permeability which attains its maximum value at the ferrimagnetic resonance frequency with concomitant minimum of Q -factor [21]. This happens due to lag of domain wall motion with the applied alternating magnetic field and is attributed to various domain defects [22], which include non-uniform and non-repetitive domain wall motion, domain wall bowing, localized variation of flux density and nucleation and annihilation of domain walls. The peak corresponding to maxima in Q -factor shifts to lower frequency range as T_s increases. Q -factor has the maximum value of 3,260 at $f = 50$ MHz for the sample sintered at 1150°C. The value of Q -factor depends on the ferrite microstructure, e.g. pore, grain size, etc.

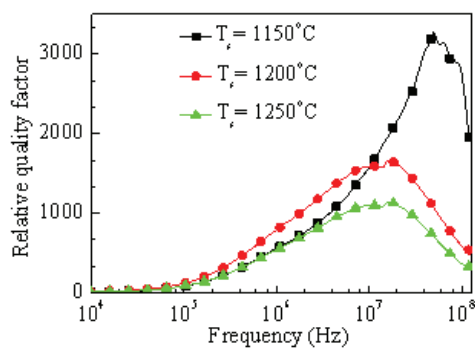


Fig. 6. Frequency dependence Relative Quality Factor for $\text{Co}_{0.4}\text{Cu}_{0.2}\text{Zn}_{0.4}\text{Fe}_2\text{O}_4$ samples sintered at 1150, 1200 and 1250 °C.

3.3 Impedance Analysis

Impedance spectroscopy is ideal for investigating the electrical response of ceramic materials as a function of frequency. It is a powerful technique for unravelling the complexities of materials, whose properties and applications depend on the close control of structure, composition, ceramic texture, dopants (or defects) and dopant distribution. The impedance analysis of a material is based on an idealized circuit model with discrete electrical components. The analysis is mainly accomplished by fitting the impedance data to an equivalent circuit that represents the material under investigation. It has been among the most useful investigating techniques, since the impedance of grains can be separated from the other sources of impedance, namely grain boundaries and electrode effects [23].

Fig. 7(a) represents the variation of real part of impedance, Z' , as a function of frequency at room temperature. It is seen that Z' decreases as the frequency increases gradually. The maximum value of Z' is observed for the sample sintered at temperature 1150°C. The higher value of the resistance means conductivity is lowered. Fig. 7(b) shows the variation of imaginary part of the impedance, Z'' , with frequency for all samples at room temperature. It is observed that the decreases as the frequency increases and the sample sintered at 1150 °C have the maximum value of Z'' .

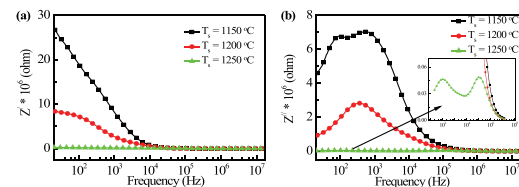


Fig. 7. The variation of (a) real part (Z') and (b) imaginary part (Z'') of impedance with frequency for $\text{Co}_{0.4}\text{Cu}_{0.2}\text{Zn}_{0.4}\text{Fe}_2\text{O}_4$ samples at room temperature sintered at 1150, 1200 and 1250 °C.

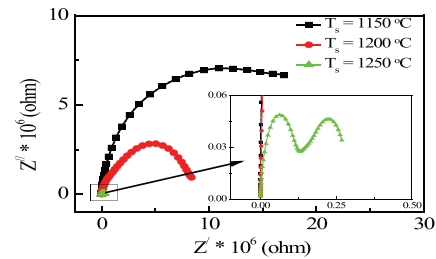


Fig. 8. Cole-Cole plot for $\text{Co}_{0.4}\text{Cu}_{0.2}\text{Zn}_{0.4}\text{Fe}_2\text{O}_4$ samples sintered at 1150, 1200 and 1250°C.

It is observed from the Cole-Cole plot for $\text{Co}_{0.4}\text{Cu}_{0.2}\text{Zn}_{0.4}\text{Fe}_2\text{O}_4$ samples in Fig. 8 that there is no complete semi-circle for the samples sintered at 1150 and 1200°C indicating that the grain boundary impedance is out of the measurement scale. The results suggest that in case of these samples the grain boundary volume is believed to be too high as compared to the grain volume. Hence, no complete semi-circle is obtained for these samples. Also, this may be due to the presence of some additional time constant, which appears outside the measured frequency range. Samples sintered at 1250°C show one full semicircle at low frequency may be due to the conduction of the grain and one incomplete semicircle at high frequency may be due to the conduction of the grain boundary. This shows that the grain boundary resistance is out of measurement scale. It also observed from Fig.8 that both grain and grain boundary resistance decreases with increasing T_s and found that the grain boundary resistance are larger than the grain resistance. This is ascribed to the fact that the atomic arrangement near the grain boundary region is disordered, resulting an increase in electron scattering. The higher boundary resistance also arises from other factors such as decrease in Fe^{2+} content in the region.

4. Conclusions

We have successfully synthesized $\text{Co}_{0.4}\text{Cu}_{0.2}\text{Zn}_{0.4}\text{Fe}_2\text{O}_4$ ferrite nanoparticles using auto combustion route. XRD results indicate that sample exhibit single phase cubic spinel structure with confirmation of crystallite size of 41 nm. FESEM micrographs show that the average grain size increase with sintering temperature. The initial permeability strongly depends on sintering temperature. The optimum sintering temperature for ferrite with improved performance is 1200°C. The samples exhibited good frequency stability within measured frequency range. The complex impedance spectra show only one semi-circle for the samples sintered at 1150 and 1200°C corresponding to the grain boundary resistance which suggests the dominance of grain boundary resistance. The complex impedance measurements show two semicircles for the sample sintered at 1250°C that indicates the resistive properties of the samples which are associated with the grain and grain boundaries.

Acknowledgement

The authors would like to express their gratitude to Dr. Md. Abdul Gafur, Senior Scientific Officer, (PP

& PDC) BCSIR, Dhaka for providing hydraulic press, oven and furnace facility and CUET authority for giving all sorts of facilities.

References

- [1] C. Sujatha, K.V. Reddy, K.S. Babu, A.R.C. Reddy and K.H.Rao, *Ceram. Inter.* 38, 5813 (2012).
- [2] K. Raj, R. Moskowitz and R. Casciari, *J. Magn. Magn. Mater.* 149, 174 (1995).
- [3] T. Tsutaoka, T. Kasagi and K. Hatakeyama, *J. Eur. Ceram. Soc.* 19, 1531 (1999).
- [4] M.M. Eltabey and N.A. Ali, *Int. J. Adv. Res.* 2, 184 (2014).
- [5] A. Tawfic, I.M. Hamada and O.M. Hamed, *J. Magn. Magn. Mater.* 250, 77 (2002).
- [6] S. Singhal, R. Sharma, T. Namgyal, S. Jauhar, S. Bhukal and J. Kaur, *Ceram. Int.* 38, 2773 (2012).
- [7] S.R. Ahmed and P. Kofinas, *Macromolecules* 35, 3338 (2002).
- [8] V.G. Patil, S.E. Shirsath, S.D. More, S.J. Shukla and K.M. Jadhav, *J. Alloys Compd.* 488, 199 (2009).
- [9] R. Arulmurugan, B. Jeyadevan, G. Vaidyanathan and S. Sendhilnathan, *J. Magn. Magn. Mater.* 288, 470 (2005).
- [10] G.V. Duong, N. Hanh, D.V. Linh, R. Groessinger, P. Weinberger, E. Schafner and M. Zehetbauer, *J. Magn. Magn. Mater.* 311, 46 (2007).
- [11] S.B. Waje, M. Hashim, W.D.W. Yousoff and Z. Abbas, *J. Magn. Magn. Mater.* 322, 686 (2010).
- [12] G. Vaidyanathan, S. Sendhilnathan and R. Arulmurgan, *J. Magn. Magn. Mater.* 313, 293 (2007).
- [13] S. Singhal, T. Namgyal, S. Bansal and K. Chandra, *J. Electromagn. Anal. Appl.* 2, 376 (2010).
- [14] S. Sindhu and D.D. Birajdar, *IOSR J. Appl. Phys.* 3, 33 (2013).
- [15] M. Ahmad, I. Ali, F. Aen, M.U. Islam, M.N. Ashiq, S. Atiq, W. Ahmad and M.U. Rana, *Ceram. Int.* 38, 1267 (2012).
- [16] B. Japes, K.S. Ashim and M. Aravind, *Sintering and surface microstructure of Ni-Zn ferrites (ICF Proc. 8)* eds M. Abe and Y. Yamazaki (Koyoto and Tokyo, Japan: ICF) PP-536 (2000).
- [17] K.S. Amarendra, T.C. Goel and R.G. Mendiratta, *Phys. Stat. Sol.* 201, 1453 (2004).

- [18] K. Venkateswarlu, A. Chandra Bose and N. Rameshbabu, *Physica B* 405, 4256 (2010).
- [19] J. Smit and H.P.J. Wijn, *Ferrites* (Philips Tech. Library, Netherlands) (1959).
- [20] A. Globus, P. Duplex and M. Guyot, *IEEE Trans. Magn.* MAG-7, 617 (1971).
- [21] F.G. Brockman, P.H. Dowling and W.G. Steneck, *Phys. Rev.* 77, 85 (1950).
- [22] K.J. Overshott, *IEEE Trans. Magn.* 17, 2698 (1981).
- [23] M. Hashim, Alimuddin, S. Kumar, S. Ali, B.H. Koo, H. Chung and R. Kumar, *J. Alloys Compd.* 511, 107 (2012).